Auto-catalytic formation of high entropy alloy nanoparticles

N. L. N. Broge, M. Bondesgaard, F. Søndergaard-Pedersen, M. Roelsgaard, B. B. Iversen*

Center for Materials Crystallography, Department of Chemistry & iNano, Aarhus University, DK-8000 Aarhus C, Denmark

*Corresponding author: bo@chem.au.dk

Abstract

High entropy alloy (HEA) nanoparticles hold great promise as tunable catalysts and surprisingly Pt-Ir-Pd-Rh-Ru nanoparticles can be synthesized under benign low-temperature solvothermal conditions. Considering that alloy formation typically is difficult in oxygen rich environments, it is peculiar that five different metals can be simultaneously reduced and alloyed in a highly complex solvent reaction. Here *in situ* X-ray scattering and transmission electron microscopy reveal the solvothermal formation mechanism of Pt-Ir-Pd-Rh-Ru nanoparticles. For the individual metal acetylacetonate precursors, formation of single metal nanoparticles takes place at temperatures spanning from ~150°C for Pd to ~350°C for Ir. However, for the mixture, homogenous Pt-Ir-Pd-Rh-Ru HEA nanoparticles can be obtained around 200°C due to autocatalyzed metal reduction at the (111) facets of the forming crystallites. The autocatalytic formation mechanism suggests that many types of HEA nanocatalysts are accessible with scalable solvothermal reactions thereby providing the essential broad availability and tunability needed to fulfil the promises.

High Entropy Alloys (HEAs) have unique properties with rich possibilities for atomic scale tuning.[1] For bulk HEAs exceptional mechanical properties (yield strength, ductility, and hardness) have been predicted and demonstrated,[1a, 2] but also hydrogen storage capacity,[3] thermoelectric properties,[4] superconductivity,[5] and the concept of pseudo-elements[6] have been explored. Nanostructured HEAs are of immense interest in heterogeneous catalysis,[7] and remarkable results for challenging reactions such as reduction of oxygen[8] or CO_2,[9] oxidation of methanol,[10] formic acid,[11] or CO,[8a] and ammonia decomposition[12] have been reported. Not only the multitude of different surface sites contribute to the outstanding properties but also strained local metal environments,[13] metal ligand effects,[14] and enhanced chemical stability compared to individual metals.[1c, 8c] With their multi-component nature, HEAs constitute a playground for the materials scientist, where variation in components, stoichiometry, and crystal structure allows for realization of unique properties and tuning toward specific applications.

While melt-based methods (arc-melting, casting, zone melting, laser cladding) have proven useful in producing bulk HEAs,[1a, 2a, 4-5, 15] the high temperatures applied are not suitable for obtaining nano-sized products, and additional synthesis steps such as ball-milling[16] or partial dealloying[8a] are necessary. Singh *et al.* produced HEA nanoparticles at relatively low temperature ($\approx 298^{\circ}C$) using reflux synthesis, but this requires use of complex (and harsh) chemicals such as benzyl ether, oleylamine and lithium triethylborohydride, and the process has limited control of product composition.[17] A different approach is to expose a precursor-impregnated carrier material to extremely high heating and cooling rates, and this has proven successful in obtaining small, homogeneous, and thermodynamically unstable nanoparticles.[8c, 12, 18] However, the method is limited in the choice of carrier material since this must be electrically conducting, have a large surface area, and be able to withstand the shock heating. Magnetron sputtering has been utilized for obtaining HEA thin films or nanoparticles, either using multiple targets in a co-sputtering process or a single target composed of pressed metal powders.[8b, 19] Recently, a general environmentally benign, simple and scalable solvothermal autoclave process was developed for HEA

nanoparticles using reaction temperatures as low as 200 °C.[20] Formation of HEAs from metal salt precursors necessarily involves reduction of the metals, and it is intriguing that acetylacetonate precursors of five widely different metals such as Pt, Ir, Pd, Rh and Ru can be simultaneously reduced and merged into a homogenous nanoparticle.

Here we investigate the formation mechanism of PtIrPdRhRu nanoparticles in solvothermal synthesis using *in situ* X-ray diffraction and Scanning Transmission Electron Microscopy coupled with Energy Dispersive Spectroscopy (STEM-EDS). The present *in situ* X-ray scattering studies use a miniature solvothermal reactor in the form of a fused silica capillary.[21] A synthesis of PtIrPdRhRu HEAs was conducted at 200°C for 77 minutes of synthesis time, Figure 1. A homogeneous distribution of all five elements is evident in the large particle in the STEM-EDS images. In the regions with smaller particles, the stoichiometries vary e.g. with a Pd-rich tail in the lower left (see the supporting information for additional images). Thus, capillary HEA solvothermal synthesis is possible, but the product is slightly inhomogeneous with a minor fraction of particles deviating from the main HEA phase. The large particles consist of agglomerated crystallites, and the particles increase in size and density with increasing reaction time (see S3 and S8). It is likely that small primary particles are formed, and extended reaction times are required for these to agglomerate and merge, as recently observed in the formation of epitaxial Pd-Pt core-shell particles from metal acetylacetonates.[22]
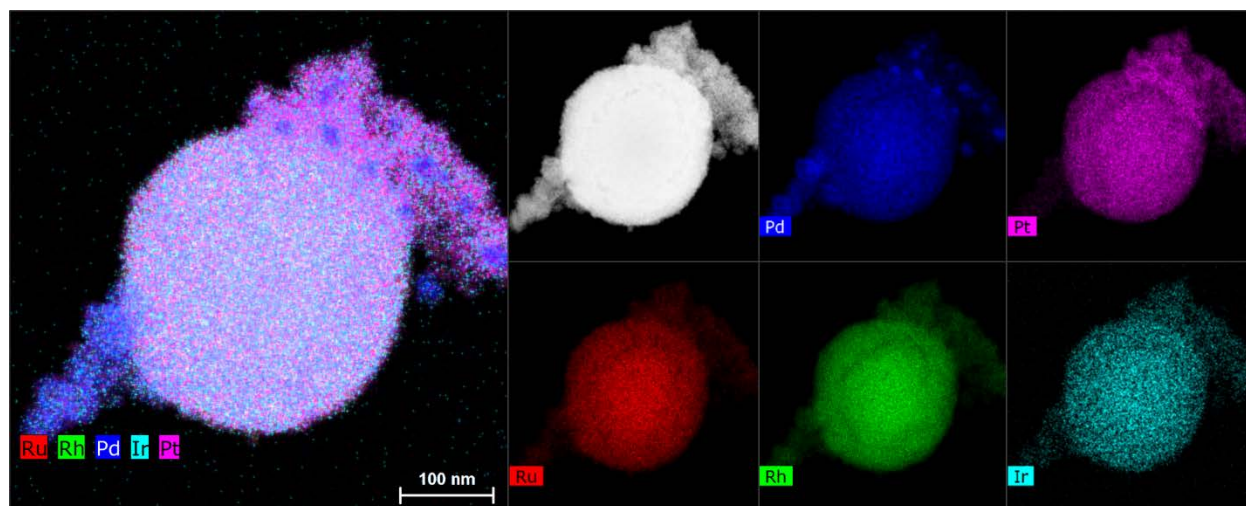
Figure 1. STEM-EDS analysis of a sample synthesized in the *in situ* reactor at 200°C for 77 minutes.

The *in situ* X-ray scattering data show that the alloy adopts a face centered cubic (fcc) structure with a unit cell length of 3.84 Å, see Figure 2. Sequential Rietveld refinements (see details in the SI) show that the formation of crystalline material is slow and the 77 min. of synthesis time used here is not sufficient for the refined scale factor to stabilize and thereby indicate a complete reaction. Initially, a sudden increase in scale factor and a simultaneous decrease in unit cell parameter from approx. 3.96 Å to 3.84 Å is observed. After ~10 min., the unit cell parameter stabilizes while the scale factor increases steadily. The constant unit cell parameter between 10 and 77 min. suggests that the composition of the growing crystalline nanoparticles does not change, and the five constituent metal precursors therefore at this point precipitate at constant rates. The initial decrease of the unit cell parameter indicates that the metals with larger unit cells (Pd, Pt) are overrepresented in the early stages of the synthesis.
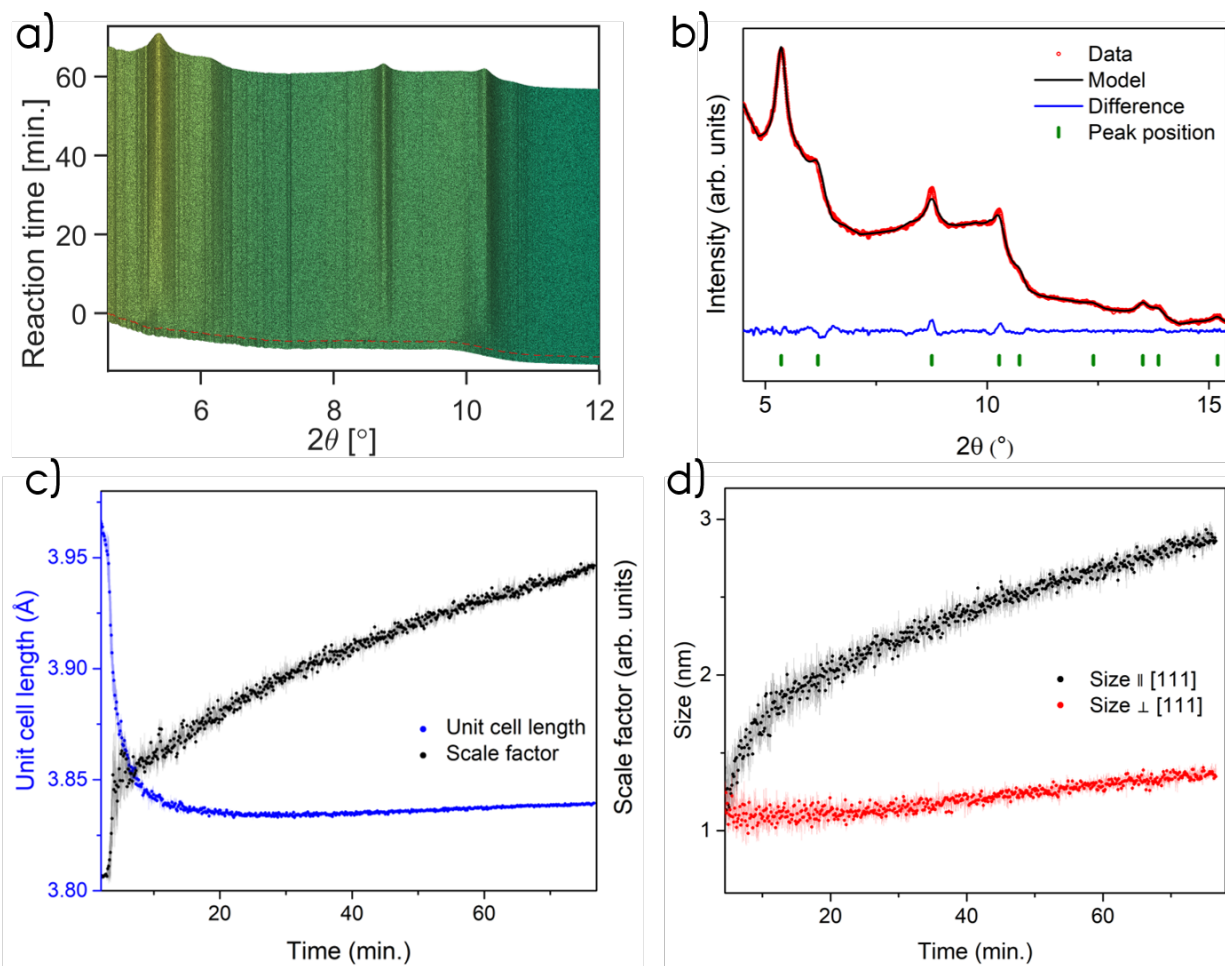
Figure 2. Results from sequential refinements of *in situ* X-ray scattering data. a) Time resolved X-ray diffraction data, b) I_{obs} - I_{calc} diagram after Rietveld refinement of the final diffractogram, (c) development of the unit cell parameter and scale factor, (d) average crystallite sizes.

Only peaks originating from the fcc phase are observed throughout the experiment. Analysis of the peak broadening (corrected for instrumental effects) provides an estimate of the volume averaged size of the coherently scattering domains (crystallites). Other broadening effects that are not accounted for in this analysis due to data quality, *e.g.* strain, will lead to underestimated absolute values of the crystallite sizes, but importantly the *in situ* data provide very reliable estimates of the relative changes.[23] The apparent average crystallite size with respect to synthesis time exhibits preferential growth along the

[111]-direction, Figure 2d. Initially the growth rate along the [111] direction is high but it stabilizes to a linear increase in size after approx. 20 min. The size and growth rate along the perpendicular direction are much smaller, and thus the particles become increasingly elongated. Bright field TEM analysis of the product shows small crystallites of around 3-15 nm in size on the edges of the large agglomerate particles (Figure S8).

In order to understand the individual metal ion reductions *in situ* X-ray total scattering data were collected in separate experiments with precursors containing only one metal species. In these experiments the reaction temperature was increased in steps of 50°C from room temperature to 450°C to find the approximate metal reduction temperatures where metallic nanoparticles form. As seen in Figure 3 there are significant differences in the temperatures for metal nanoparticle formation with a span from 150°C for Pd to 350°C for Ir. From these data it is indeed intriguing that HEA nanoparticles are observed both *ex situ* and *in situ* for the reaction at 200°C with a mix of five metal acetylacetonate precursors.
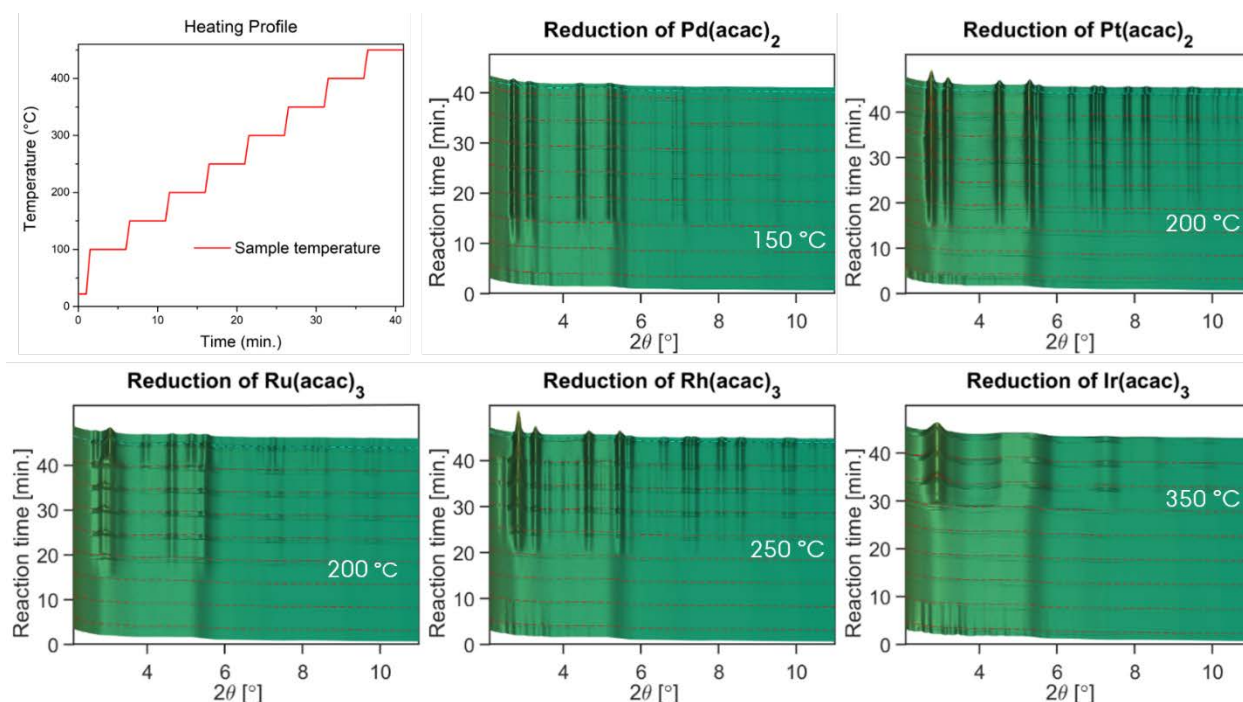
Figure 3. Time-resolved X-ray scattering data from experiments with single metal acetylacetonate precursors. The heating profile for the experiments is plotted in the top left, and the heating steps are marked with red dashed lines for each dataset. The lowest reaction temperatures at which Bragg peaks are observed are indicated on the plots. Note that Bragg peaks from undissolved metal acetylacetonate reactant are observed at room temperature, but these peaks disappear between 100°C to 150°C indicating complete dissolution and thus homogenous precursor solutions.

The X-ray total scattering data from the dissolved precursors were background corrected, scaled and Fourier transformed to obtain Pair Distribution Functions (PDFs) as shown Figure 4. Similar structural features are observed for all metal precursor solutions with distinct peaks below 3 Å (note enlargement in the figure) and weak correlations at longer interatomic distances. The peaks below 3 Å correspond to interatomic distances within a metal acetylacetonate complex,[24] and the lack of long-range features indicates that only monomers are present.
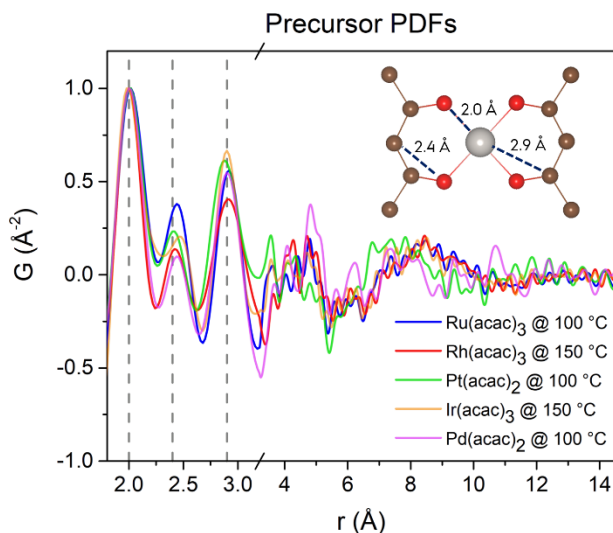

Figure 4. PDFs from dissolved metal acetylacetonates. An illustration of the $Pt(acac)_2$ monomer is inserted in the upper right with some interatomic distances indicated. The corresponding distances are marked with vertical dashed lines in the plot of the PDFs. Note the change of scale on the *x*-axis.

While the HEA nanoparticles that forms at 200°C contain all five elements, only three of them (Pd, Pt, Ru) precipitate at this temperature from their individual precursor solutions (Figure 3). This suggests that the initially formed metal nanoparticles catalyze the reduction of the other metal ions, and that this "auto-catalytic" activity is maintained for the continuously growing HEA nanoparticle. As shown in Figure 2 the nanoparticles have a strongly preferred growth along the [111] direction meaning that the (111) crystal facets are the catalytically active in the process. At 200°C it appears that the autocatalyzed reduction temperatures of the different metals are almost balanced such that any metal atom near the surface will be involved in growth of the particle. It would be of considerable interest to probe the crystal growth mechanism at atomic scale using theoretical modelling. Considering that low-temperature solvothermal synthesis has only been demonstrated using acetylacetonate precursors and that monomer complexes are present prior to reduction, it is plausible that interactions between the bidentate acetylacetonate ligand and the active surface play a key role in the process.

Since Pd has the lowest precipitation temperature it is likely to form the initial nuclei. To support this hypothesis, an *in situ* experiment was performed at 150°C. An alloy with all five constituents was obtained at an extended reaction time of 72 min. as seen in Figure 5, although with an increased fraction of Pd and lower contents of Ru and Ir. This means that the reduction of the other metal ions must be auto-catalyzed by the initial Pd nuclei, but with uneven reduction rates for the different metal ions at the low synthesis temperature of 150°C. Experiments with reaction temperatures at 300°C and 437°C yield products containing all five metals, but still with inhomogeneous distributions in the particles as seen in Figure 5. Pd is concentrated in the core of the particles, while the shell primarily consists of Ir reflecting the higher and lower reduction temperatures for Pd^{2+} and Ir^{3+}, respectively. Phase splitting is observed in the PXRD data, and the peaks of the main fcc phase display shoulders caused by crystalline domains with different lattice parameters (Figure 5d). Additional peaks appear at the highest temperature. This matches

the findings of Mi *et al*., where Ru crystallizes in a fcc structure at low reaction temperatures (≤250°C), but in an hcp structure at higher reaction temperatures under similar synthesis conditions as used here.[25]
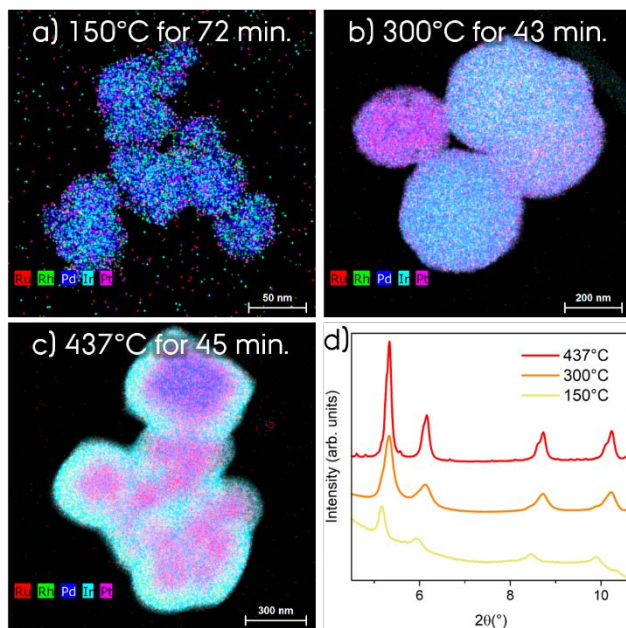

Figure 5. a)-c) STEM-EDS elemental maps of samples synthesized at different reaction temperatures. d) Corresponding diffractograms from the *in situ* X-ray data.

The combined data show that the formation of HEA nanoparticles is influenced by both time and temperature. The temperature window for synthesis of homogeneous PtIrPdRhRu HEA nanoparticles is relatively narrow around 200°C. At higher temperatures (≥ 300°C) phase splitting is observed, while sample inhomogeneity and element deficiency is seen at lower temperature. Because of the low temperature of 200°C, relatively long reaction times of hours are necessary for full conversion of the reactants. Overall, the formation mechanism for the PtIrPdRhRu nanoparticles can be summarized as in Figure 6.
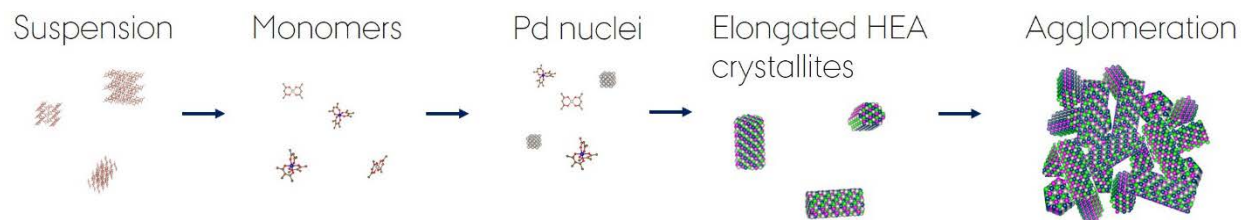
Figure 6. Schematic representation of the formation mechanism for PtIrPdRhRu HEA nanoparticles under solvothermal conditions.

In summary, we have used *in situ* X-ray scattering experiments to follow the nucleation and growth of PtIrPdRhRu high entropy alloy nanoparticles. Homogenous materials are obtained in a relatively narrow temperature window around 200°C, which is much lower than the reduction temperature of some of the metals in single precursor solvothermal reactions. The HEA nanoparticles form from an initial Pd core that autocatalyzes the reduction of the other metals primarily on the (111) facets of the growing nanocrystals. The auto-catalytic activity is maintained throughout the reaction resulting in crystallites with elongated morphology. The autocatalysis means that the alloying is a kinetically driven process where metal incorporation is governed by the reduction rates and not the thermodynamic energy gain of mixing. This means that the method presumably is not limited to the formation of thermodynamically stable alloys, and therefore may allow production of novel materials with unique properties.

Experimental Section

Details on the used chemicals, *in situ* X-ray scattering data collection, reactor heating profiles, Rietveld refinement, PDF modelling, and additional TEM data are provided in the Supporting Information.

Acknowledgements

References

[1] a) J.-W. Yeh, S.-K. Chen, S.-J. Lin, T.-T. Gan, T.-S. Chin, T.-T. Shun, C.-H. Tsau, S.-Y. Chang*, Adv. Eng. Mater.* **2004**, *6*, 299; b) M.-H. Tsai, J.-W. Yeh*, Mater. Res. Lett.* **2014**, *2*, 107; c) D. B. Miracle, O. N. Senkov*, Acta Mater.* **2017**, *122*, 448)

[2] a) S. Sohn, Y. Liu, J. Liu, P. Gong, S. Prades-Rodel, A. Blatter, B. E. Scanley, C. C. Broadbridge, J. Schroers*, Scr. Mater.* **2017**, *126*, 29; b) C. Varvenne, W. A. Curtin*, Scr. Mater.* **2018**, *142*, 92

[3] a) Y.-F. Kao, S.-K. Chen, J.-H. Sheu, J.-T. Lin, W.-E. Lin, J.-W. Yeh, S.-J. Lin, T.-H. Liou, C.-W. Wang*, Int. J. Hydrog. Energy* **2010**, *35*, 9046; b) M. Sahlberg, D. Karlsson, C. Zlotea, U. Jansson*, Sci. Rep.* **2016**, *6*, 36770

[4] S. Shafeie, S. Guo, Q. Hu, H. Fahlquist, P. Erhart, A. Palmqvist*, J. Appl. Phys.* **2015**, 118, 184905

[5] P. Kozelj, S. Vrtnik, A. Jelen, S. Jazbec, Z. Jaglicic, S. Maiti, M. Feuerbacher, W. Steurer, J. Dolinsek*, Phys. Rev. Lett.* **2014**, *113*, 107001

[6] A. P. Tsai, S. Kameoka, K. Nozawa, M. Shimoda, Y. Ishii*, Acc. Chem. Res.* **2017**, *50*, 2879

[7] a) T. Löffler, A. Savan, A. Garzón-Manjón, M. Meischein, C. Scheu, A. Ludwig, W. Schuhmann*, ACS Energy Lett.* **2019**, *4*, 1206; b) T. A. A. Batchelor, J. K. Pedersen, S. H. Winther, I. E. Castelli, K. W. Jacobsen, J. Rossmeisl*, Joule* **2019**, *3*, 834; c) J. K. Pedersen, T. A. A. Batchelor, A. Bagger, J. Rossmeisl*, ACS Catal.* **2020**, *10*, 2169

[8] a) H.-J. Qiu, G. Fang, Y. Wen, P. Liu, G. Xie, X. Liu, S. Sun*, J. Mater. Chem. A* **2019**, *7*, 6499; b) T. Löffler, H. Meyer, A. Savan, P. Wilde, A. Garzón Manjón, Y.-T. Chen, E. Ventosa, C. Scheu, A. Ludwig, W. Schuhmann*, Adv. Energy Mater.* **2018**, *8*, 1802269; c) S. D. Lacey, Q. Dong, Z. Huang, J. Luo, H. Xie, Z. Lin, D. J. Kirsch, V. Vattipalli, C. Povinelli, W. Fan, R. Shahbazian-Yassar, D. Wang, L. Hu*, Nano Lett.* **2019**, *19*, 5149

[9] S. Nellaiappan, N. K. Katiyar, R. Kumar, A. Parui, K. D. Malviya, K. G. Pradeep, A. K. Singh, S. Sharma, C. S. Tiwary, K. Biswas*, ACS Catal.* **2020**, *10*, 3658

[10] A.-L. Wang, H.-C. Wan, H. Xu, Y.-X. Tong, G.-R. Li*, Electrochim. Acta* **2014,** *127*, 448

[11] N. K. Katiyar, S. Nellaiappan, R. Kumar, K. D. Malviya, K. G. Pradeep, A. K. Singh, S. Sharma, C. S. Tiwary, K. Biswas*, Mater. Today Energy* **2020**, *16*, 100393

[12] P. Xie, Y. Yao, Z. Huang, Z. Liu, J. Zhang, T. Li, G. Wang, R. Shahbazian-Yassar, L. Hu, C. Wang*, Nat. Commun.* **2019**, *10*, 4011

[13] L. Bu, N. Zhang, S. Guo, X. Zhang, J. Li, J. Yao, T. Wu, G. Lu, J.-Y. Ma, D. Su, X. Huang*, Science* **2016**, *354*, 1410

[14] a) T. Bligaard, J. K. Nørskov*, Electrochim. Acta* **2007**, *52*, 5512 (2007); b) A. Holewinski, J. C. Idrobo, S. Linic*, Nat. Chem.* **2014**, *6*, 828

[15] a) G. Zhang, K. Ming, J. Kang, Q. Huang, Z. Zhang, X. Zheng, X. Bi*, Electrochim. Acta* **2018**, *279*, 19; b) H. Zhang, Y. Pan, Y. He, H. Jiao*, Appl. Surf. Sci.* **2011**, *257*, 2259

[16]   a) X. Chen, C. Si, Y. Gao, J. Frenzel, J. Sun, G. Eggeler, Z. Zhang, *J. Power Sources* **2015**, *273*, 324; b) Z. Y. Lv, X. J. Liu, B. Jia, H. Wang, Y. Wu, Z. P. Lu, *Sci Rep* **2016**, *6*, 34213; c) A. J. Zaddach, C. Niu, C. C. Koch, D. L. Irving, *JOM* **2013**, *65*, 1780; d) N. Kumar, C. S. Tiwary, K. Biswas, *J. Mater. Sci.* **2018**, *53*, 13411

[17]   M. P. Singh, C. Srivastava, *Mater. Lett.* **2015**, *160*, 419

[18]   a) Y. Yao, Z. Huang, P. Xie, S. D. Lacey, R. J. Jacob, H. Xie, F. Chen, A. Nie, T. Pu, M. Rehwoldt, D. Yu, M. R. Zachariah, C. Wang, R. Shahbazian-Yassar, J. Li, L. Hu, *Science* **2018**, *359***,** 1489; b) M. W. Glasscott, A. D. Pendergast, S. Goines, A. R. Bishop, A. T. Hoang, C. Renault, J. E. Dick, *Nat. Commun.* **2019**, *10*, 2650

[19]   a) C.-F. Tsai, K.-Y. Yeh, P.-W. Wu, Y.-F. Hsieh, P. Lin, *J. Alloys Compd.* **2009**, *478*, 868; b) A. Marshal, K. G. Pradeep, D. Music, S. Zaefferer, P. S. De, J. M. Schneider, *J. Alloys Compd.* **2017**, *691*, 683; c) A. Marshal, K. G. Pradeep, D. Music, L. Wang, O. Petracic, J. M. Schneider, *Sci Rep* **2019**, *9*, 7864; d) S. Fritze, C. M. Koller, L. von Fieandt, P. Malinovskis, K. Johansson, E. Lewin, P. H. Mayrhofer, U. Jansson, *Materials* **2019**, *12*

[20]   M. Bondesgaard, N. L. N. Broge, A. Mamakhel, M. Bremholm, B. B. Iversen, *Adv. Funct. Mater.* **2019**, *29*, 1905933

[21]   J. Becker, M. Bremholm, C. Tyrsted, B. Pauw, K. M. Ø. Jensen, J. Eltzholt, M. Christensen, B. B. Iversen, *J. Appl. Crystallogr.* **2010**, *43*, 729

[22]   N. L. N. Broge, F. Søndergaard-Pedersen, S. Sommer, B. B. Iversen, *Adv. Funct. Mater.* **2019**, *29*, 1902214

[23]   H. L. Andersen, E. D. Bøjesen, S. Birgisson, M. Christensen, B. B. Iversen, *J. Appl. Crystallogr.* **2018**, *51*, 526

[24]   D. Saha, E. D. Bøjesen, A. H. Mamakhel, M. Bremholm, B. B. Iversen, *ChemNanoMat* **2017**, *3*, 472

[25]   J.-L. Mi, Y. Shen, J. Becker, M. Bremholm, B. B. Iversen, *J. Phys. Chem. C* **2014**, *118*, 11104

[26]   A. C. Dippel, H. P. Liermann, J. T. Delitz, P. Walter, H. Schulte-Schrepping, O. H. Seeck, H. Franz, *J. Synchrotron Radiat.* **2015**, *22*, 675